

Efficient photon triplet generation in integrated nanophotonic waveguides

Michael G. Moebius,¹ Felipe Herrera,^{2,3} Sarah Griesse-Nascimento,¹
Orad Reshef,¹ Christopher C. Evans,^{1,4} Gian Giacomo Guerreschi,³
Alán Aspuru-Guzik,³ and Eric Mazur^{1,*}

¹John A. Paulson School of Engineering and Applied Sciences, Harvard University,
Cambridge, Massachusetts 02138, USA

²Department of Physics, Universidad de Santiago de Chile, Av. Ecuador 3943, Santiago, Chile

³Department of Chemistry and Chemical Biology, Harvard University, 12 Oxford St.,
Cambridge, Massachusetts 02138, USA

⁴Current address: Kavli Institute at Cornell for Nanoscale Science, Cornell University, Ithaca,
New York 14853, USA

*mazur@seas.harvard.edu

Abstract: Generation of entangled photons in nonlinear media constitutes a basic building block of modern photonic quantum technology. Current optical materials are severely limited in their ability to produce three or more entangled photons in a single event due to weak nonlinearities and challenges achieving phase-matching. We use integrated nanophotonics to enhance nonlinear interactions and develop protocols to design multimode waveguides that enable sustained phase-matching for third-order spontaneous parametric down-conversion (TOSPDC). We predict a generation efficiency of 0.13 triplets/s/mW of pump power in TiO₂-based integrated waveguides, an order of magnitude higher than previous theoretical and experimental demonstrations. We experimentally verify our device design methods in TiO₂ waveguides using third-harmonic generation (THG), the reverse process of TOSPDC that is subject to the same phase-matching constraints. We finally discuss the effect of finite detector bandwidth and photon losses on the energy-time coherence properties of the expected TOSPDC source.

© 2016 Optical Society of America

OCIS codes: (190.4390) Nonlinear optics, integrated optics; (190.4410) Nonlinear optics, parametric processes; (270.4180) Quantum optics, multiphoton processes.

References and links

1. J. L. O'Brien, A. Furusawa, and J. Vučković, "Photonic quantum technologies," *Nat. Photonics* **3**, 687–695 (2009).
2. Z.-S. Yuan, X.-H. Bao, C.-Y. Lu, J. Zhang, C.-Z. Peng, and J.-W. Pan, "Entangled photons and quantum communication," *Phys. Rep.* **497**, 1–40 (2010).
3. V. Giovannetti and S. Lloyd, "Advances in quantum metrology," *Nat. Photonics* **5**, 222–229 (2011).
4. L. Lugiato, A. Gatti, and E. Brambilla, "Quantum imaging," *J. Opt. B: Quantum Semiclassical Opt.* **4**, S176 (2002).
5. M. A. Taylor, J. Janousek, V. Daria, J. Knittel, B. Hage, H.-a. Bachor, and W. P. Bowen, "Biological measurement beyond the quantum limit," *Nat. Photonics* **7**, 229–233 (2013).
6. M. G. Raymer, A. H. Marcus, J. R. Widom, and D. L. P. Vitullo, "Entangled photon-pair two-dimensional fluorescence spectroscopy," *J. Phys. Chem. B* **117**, 15559–15575 (2013).
7. T. D. Ladd, F. Jelezko, R. Laflamme, Y. Nakamura, C. Monroe, and J. L. O'Brien, "Quantum computers," *Nature* **464**, 45 (2010).

8. Y. Shih, "Entangled biphoton source—property and preparation," *Rep. Prog. Phys.* **66**, 1009–1044 (2003).
9. A. Dousse, J. Suffczynski, A. Beveratos, O. Krebs, A. Lemaître, I. Sagnes, J. Bloch, P. Voisin, and P. Senellart, "Ultrabright source of entangled photon pairs," *Nature* **466**, 217–220 (2010).
10. Q. Lin, F. Yaman, and G. P. Agrawal, "Photon-pair generation in optical fibers through four-wave mixing: role of Raman scattering and pump polarization," *Phys. Rev. A: At. Mol. Opt. Phys.* **75**, 023803 (2007).
11. A. M. Lance and T. Symul and W. P. Bowen and B. C. Sanders and P. K. Lam "Tripartite quantum state sharing," *Phys. Rev. Lett.* **92**, 177903 (2004).
12. M. Gimenó-Segovia and P. Shadbolt and D. E. Browne and T. Rudolph "From three-photon Greenberger-Horne-Zeilinger states to ballistic universal quantum computation," *Phys. Rev. Lett.* **115**, 020502 (2015).
13. H. Hubel, D. R. Hamel, A. Fedrizzi, S. Ramelow, K. J. Resch, and T. Jennewein, "Direct generation of photon triplets using cascaded photon-pair sources," *Nature* **466**, 601–603 (2010).
14. L. K. Shalm, D. R. Hamel, Z. Yan, C. Simon, K. J. Resch, and T. Jennewein, "Three-photon energy-time entanglement," *Nat. Phys.* **9**, 19–22 (2012).
15. D. R. Hamel, L. K. Shalm, H. Hübel, A. J. Miller, F. Marsili, V. B. Verma, R. P. Mirin, S. W. Nam, K. J. Resch, and T. Jennewein, "Direct generation of three-photon polarization entanglement," *Nat. Photonics* **8**, 801–807 (2014).
16. M. Chekhova, O. Ivanova, V. Berardi, and A. Garuccio, "Spectral properties of three-photon entangled states generated via three-photon parametric down-conversion in a $\chi^{(3)}$ medium," *Phys. Rev. A: At. Mol. Opt. Phys.* **72**, 023818 (2005).
17. K. Bencheikh, F. Gravier, J. Douady, A. Levenson, and B. Boulanger, "Triple photons: a challenge in nonlinear and quantum optics," *C. R. Phys.* **8**, 206–220 (2007).
18. C. C. Evans, J. D. B. Bradley, E. A. Marti-Panadero, and E. Mazur, "Mixed two- and three-photon absorption in bulk rutile (TiO₂) around 800 nm," *Opt. Express* **20**, 3118–3128 (2012).
19. C. C. Evans, K. Shtyrkova, J. D. B. Bradley, O. Reshef, E. Ippen, and E. Mazur, "Spectral broadening in anatase titanium dioxide waveguides at telecommunication and near-visible wavelengths," *Opt. Express* **21**, 18582–18591 (2013).
20. J. D. B. Bradley, C. C. Evans, J. T. Choy, O. Reshef, P. B. Deotare, F. Parsy, K. C. Phillips, M. Loncar, and E. Mazur, "Submicrometer-wide amorphous and polycrystalline anatase TiO₂ waveguides for microphotonic devices," *Opt. Express* **20**, 23821–23831 (2012).
21. J. T. Choy, J. D. B. Bradley, P. B. Deotare, I. B. Burgess, C. C. Evans, E. Mazur, and M. Loncar, "Integrated TiO₂ resonators for visible photonics," *Opt. Lett.* **37**, 539–541 (2012).
22. C. C. Evans, K. Shtyrkova, O. Reshef, M. Moebius, J. D. B. Bradley, S. Griesse-Nascimento, E. Ippen, and E. Mazur, "Multimode phase-matched third-harmonic generation in sub-micrometer-wide anatase TiO₂ waveguides," *Opt. Express* **23**, 7832 (2015).
23. M. D. Eisaman, J. Fan, A. Migdall, and S. V. Polyakov, "Invited review article: single-photon sources and detectors," *Rev. Sci. Instrum.* **82**, 71101–71125 (2011).
24. M. Corona, K. Garay-Palmett, and A. B. U'Ren, "Third-order spontaneous parametric down-conversion in thin optical fibers as a photon-triplet source," *Phys. Rev. A: At. Mol. Opt. Phys.* **84**, 033823 (2011).
25. S. Richard, K. Bencheikh, B. Boulanger, and J. A. Levenson, "Semiclassical model of triple photons generation in optical fibers," *Opt. Lett.* **36**, 3000–3002 (2011).
26. O. Reshef, K. Shtyrkova, M. G. Moebius, S. Griesse-Nascimento, S. Spector, C. C. Evans, E. Ippen, and E. Mazur, "Polycrystalline anatase titanium dioxide micro-ring resonators with negative thermo-optic coefficient," *J. Opt. Soc. Am. B: Opt. Phys.* **32**, 2288–2293 (2015).
27. K. Preston, B. Schmidt, and M. Lipson, "Polysilicon photonic resonators for large-scale 3D integration of optical networks," *Opt. Express* **15**, 17283 (2007).
28. I. A. Bufetov, M. V. Grekov, K. M. Golant, E. M. Dianov, and R. R. Khrapko, "Ultraviolet-light generation in nitrogen-doped silica fiber," *Opt. Lett.* **22**, 1394 (1997).
29. Z. Zhu and T. Brown, "Full-vectorial finite-difference analysis of microstructured optical fibers," *Opt. Express* **10**, 853–864 (2002).
30. R. Boyd, *Nonlinear Optics*, 3rd ed. (Elsevier, Burlington, USA, 2008).
31. M. Sheik-Bahae, D. Hagan, and E. Van Stryland, "Dispersion and band-gap scaling of the electronic kerr effect in solids associated with two-photon absorption," *Phys. Rev. Lett.* **65**, 96–99 (1990).
32. T. Lee, N. G. R. Broderick, and G. Brambilla, "Resonantly enhanced third harmonic generation in microfiber loop resonators," *J. Opt. Soc. Am. B: Opt. Phys.* **30**, 505–511 (2013).
33. B. Corcoran, C. Monat, C. Grillet, D. J. Moss, B. J. Eggleton, T. P. White, L. O'Faolain, and T. F. Krauss, "Green light emission in silicon through slow-light enhanced third-harmonic generation in photonic-crystal waveguides," *Nat. Photonics* **3**, 206–210 (2009).
34. S. Krapick and C. Silberhorn, "Analysis of photon triplet generation in pulsed cascaded parametric down-conversion sources," *arXiv.org/abs/1506.07655* (2015).
35. N. Gisin and R. Thew "Quantum communication," *Nat. Photonics* **1**, 165–171 (2007).
36. J. Brendel and N. Gisin and W. Tittel and H. Zbinden "Pulsed energy-time entangled twin-photon source for quantum communication," *Phys. Rev. Lett.* **82**, 2594 (1999).

37. I. Ali-Khan and C. J. Broadbent and J. C. Howell "Large-alphabet quantum key distribution using energy-time entangled bipartite states," *Phys. Rev. Lett.* **98**, 060503 (2007).
38. Wen, J., and Rubin, M. "Distinction of tripartite Greenberger-Horne-Zeilinger and W states entangled in time (or energy) and space," *Phys. Rev. A: At. Mol. Opt. Phys.* **79**, 025802 (2009).
39. C. C. Evans, C. Liu, and J. Suntivich, "Low-loss titanium dioxide waveguides and resonators using a dielectric lift-off fabrication process," *Opt. Express* **23**, 11160 (2015).
40. M. Soljačić and J. D. Joannopoulos, "Enhancement of nonlinear effects using photonic crystals," *Nat. Mater.* **3**, 211–219 (2004).
41. Y. Watanabe, M. Ohnishi, and T. Tsuchiya, "Measurement of nonlinear absorption and refraction in titanium dioxide single crystal by using a phase distortion method," *Appl. Phys. Lett.* **66**, 3431 (1995).
42. S. K. Das, C. Schwanke, A. Pfuch, W. Seeber, M. Bock, G. Steinmeyer, T. Elsaesser, and R. Grunwald, "Highly efficient THG in TiO₂ nanolayers for third-order pulse characterization," *Opt. Express* **19**, 16985–16995 (2011).

1. Introduction

Optical quantum technologies [1] often rely on nonlinear optical crystals pumped with coherent radiation to generate light with non-classical properties, including entanglement. Entangled photons have applications in many fields, such as quantum cryptography [2], quantum metrology [3], quantum imaging [4,5], quantum spectroscopy [6], and quantum information processing [7]. Many experimental efforts aim towards the generation, manipulation, and detection of entangled photons using nanoscale optical devices that provide a compact and scalable platform to perform quantum optics experiments on a single chip [1].

Entangled states of light containing three or more photons are currently built interferometrically starting from entangled photon pairs or single photons [2], with entangled pairs typically generated via spontaneous parametric down-conversion (SPDC) [8], biexciton decay [9], and spontaneous four-wave mixing [10]. Tripartite entanglement can be used for quantum secret sharing [11] and measurement-based quantum computing [12]. The production of entangled photon triplets via cascaded SPDC has been demonstrated [13–15], with generation efficiencies on the order of 10^{-2} triplets/s/mW pump power [14]. Third-order spontaneous parametric down conversion (TOSPD), when one pump photon splits into three signal photons, can also generate entangled photon triplets. The temporal coherence properties of TOSPD photon triplets are different from cascaded SPDC sources [16].

TOSPD represents an experimental challenge [17] due to low third-order nonlinearities ($\chi^{(3)}$) in typical optical materials. Moreover, phase-matching becomes increasingly difficult to satisfy for widely-spaced wavelengths. Recently, nanoscale optical devices have emerged as a promising route to enhance nonlinear-optical processes, mostly due to high field intensity from sub-wavelength confinement of the electromagnetic field [1]. In addition, sustained phase-matching for widely-spaced wavelengths can be achieved using strong dispersion in non-fundamental waveguide modes. These remarkable improvements over bulk materials indicate that integrated nanophotonic waveguides can enable efficient TOSPD.

In this work, we propose a protocol to optimize efficient generation of entangled photon triplets via TOSPD in nanophotonic waveguides. We discuss in detail how to optimize key design parameters, such as phase-matching and mode overlap between visible pump and infrared signal modes, while also considering the impacts of photon losses. Our proposed design protocol can be applied to many waveguide materials and geometries. We validate our design protocol experimentally by demonstrating THG, the reverse of TOSPD, in nanoscale TiO₂ waveguides. Titanium dioxide (TiO₂) is a promising material platform for efficient TOSPD [18–22]. Pumping with a visible laser at $\lambda_p = 420\text{--}450\text{ nm}$ or $510\text{--}520\text{ nm}$ generates photons in the O and C telecommunication bands, allowing integration with silicon photonics, existing telecommunications infrastructure, and efficient single photon detection [23]. We finally calculate the temporal coherence properties of TOSPD sources in coincidence measurements, taking into account finite detector bandwidths and propagation losses.

2. Device design

TOSPDC in bulk nonlinear optical materials has previously been ruled out as a viable source of entangled photons due to the inherent difficulty of achieving phase-matching across nearly two octaves, low $\chi^{(3)}$ nonlinearities, and weak light confinement over long interaction lengths [17]. TOSPDC in nano-scale silica fibers was proposed theoretically by Corona et al. [24]. The predicted photon triplet generation efficiency in 10-cm long silica fibers, ignoring the impact of photon losses, is 1.9×10^{-2} triplets/s/mW of pump power [24,25], which is comparable to current experimental demonstrations [13,14]. However, silica fibers cannot be easily integrated to produce on-chip photon triplet sources due to incompatibility with CMOS fabrication techniques and low index contrast with commonly-used cladding materials.

We propose to use an alternative material, TiO_2 , for its high refractive index, high $\chi^{(3)}$ nonlinearity, and CMOS compatibility [26,27]. These characteristics make TiO_2 an excellent platform for an on-chip, integrated photon triplet source.

Optimizing the efficiency of photon triplet generation in nanophotonic waveguides requires four major considerations: phase-matching, mode overlap, interaction length, and power coupled into the phase-matched pump mode. In the rest of this section, we define criteria to optimize these factors and achieve the largest triplet generation efficiency. We consider photon losses due to their impact on conversion efficiency, optimal device length, and signal spectrum. Using optimized parameters for a TiO_2 nanoscale waveguide, we predict its performance for TOSPDC under realistic conditions, including photon losses.

2.1. Higher-order mode phase-matching

According to Fermi's golden rule [17], the transition rate for the conversion of a pump photon of frequency ω_p into three signal photons at frequencies denoted as ω_s , ω_r and ω_i is strongly suppressed for any combination of frequencies that does not satisfy the energy conservation constraint $\omega_p = \omega_r + \omega_s + \omega_i$. The probability of generating signal photons that satisfy energy conservation is maximal for those combinations that also satisfy the phase-matching or momentum-conservation rule, $\mathbf{k}_p = \mathbf{k}_r + \mathbf{k}_s + \mathbf{k}_i$, where \mathbf{k}_m is the wavevector of each photon in mode $m = \{p, s, r, i\}$. In this work, we consider nanoscale ridge waveguides (Fig. 1(b)), for which the propagation direction of guided modes is along the waveguide. In this case, momentum conservation reduces to a scalar identity for the magnitude of the wavenumbers of propagating modes $k = 2\pi n_{\text{eff}}/\lambda$, where n_{eff} is the effective refractive index of the signal mode at wavelength λ .

The wavelength dependence of the effective index $n_{\text{eff}}(\lambda)$ in guided modes is determined by the waveguide geometry, dispersion properties of the core and cladding materials, and mode order. In the optical regime, the refractive index for a transparent material is typically larger at the shortest wavelengths, monotonically decreasing with increasing wavelength. For example, in TiO_2 there is an index mismatch of 0.17 between a 532-nm pump and 1596-nm signal wavelength, which leads to a 1.6- μm coherence length. Additionally, for a given wavelength λ , higher-order modes have a lower effective index than the fundamental mode. In Fig. 1(a), we demonstrate these two points by plotting the effective index for two modes (*i.e.*, the TM_{00} fundamental [signal] and TM_{02} higher-order [pump] modes) of a TiO_2 waveguide with a 550-nm core width and a 360-nm thickness, with an SiO_2 cladding. By employing a higher-order mode at the shorter wavelength, we can match effective indices for highly disparate wavelengths [22,28].

We define the perfect phase matching (PPM) point as the pump wavelength λ_p^0 for which $n_{\text{eff}}^s(3\lambda_p^0) = n_{\text{eff}}^p(\lambda_p^0)$, where n_{eff}^s is the effective index of the signal mode of interest and n_{eff}^p is the pump index. At the PPM point, the phase-matching condition reads $k_p^0 = 3k_s^0$, since all three signal photon frequencies are degenerate. For the case of a monochromatic pump at the PPM-

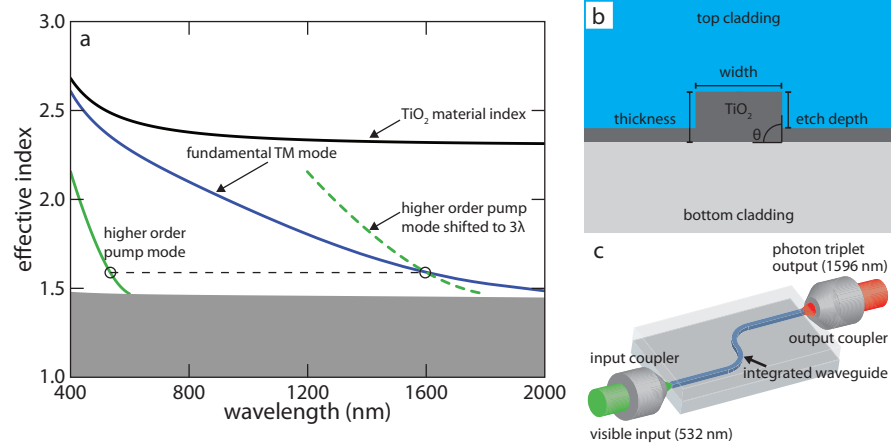


Fig. 1. (a) Schematic of higher-order mode phase matching using calculated dispersion data for a fully-etched 550×360 nm TiO₂ waveguide with SiO₂ cladding. Shifting the pump mode from λ_p to $3\lambda_p$ gives a point of intersection where the effective indices of the TM₀₀ signal and TM₀₂ pump modes are the same. Phase matching is achieved at $\lambda_p = 532$ nm. Guided modes reach a cutoff wavelength when their effective index is equal to the cladding SiO₂ index (gray region). (b) Schematic of the waveguide cross section and tunable parameters. (c) 3D schematic of an integrated device with input and output coupling.

condition, the signal photons can be generated away from $\omega_p/3$, so long as energy conservation is maintained. A finite phase-mismatch will result from group velocity dispersion (GVD) in the signal mode ($D_s = \partial^2 k_s / \partial \omega_s^2 |_{\omega_s = \omega_s^0}$), limiting the bandwidth. The signal bandwidth at PPM is thus given by Δ_{PPM} , corresponding to the FWHM of the function $\text{sinc}^2(\Delta k L / 2)$, which determines the triplet generation rate as a function of finite phase mismatch (see Section 2.3):

$$\Delta_{\text{PPM}} = \sqrt{\frac{4\pi}{L|D_s|}} \quad (1)$$

where L is the nonlinear interaction length. The relative intensities of the signal photons that are emitted for the PPM case are visualized in Fig. 2(a), where the idler (ω_i) vs. signal-frequency (ω_s) intensity-plot shows a single peak centered at the degenerate signal frequency. The black curve in Fig. 2(d) shows the corresponding intensity of all three signal photons as a function of frequency.

In TOSPD, the pump wavelength can be blue-detuned away from the PPM point while still satisfying energy and momentum conservation efficiently for normal signal-mode dispersion. This produces non-degenerate photon triplets in energy. Energy and momentum conservation cannot simultaneously be satisfied for a red-detuned pump with normal dispersion in the signal mode. Satisfying energy and momentum conservation rules for 1D propagation results in an under-constrained system of equations with two free parameters. One is fixed by choosing the pump frequency $\omega_p = 2\pi c / \lambda_p$. We can choose the remaining degree of freedom to be one of the signal frequencies ω_m , with $m = \{s, r, i\}$.

We refer to the range of signal frequencies over which energy and momentum conservation

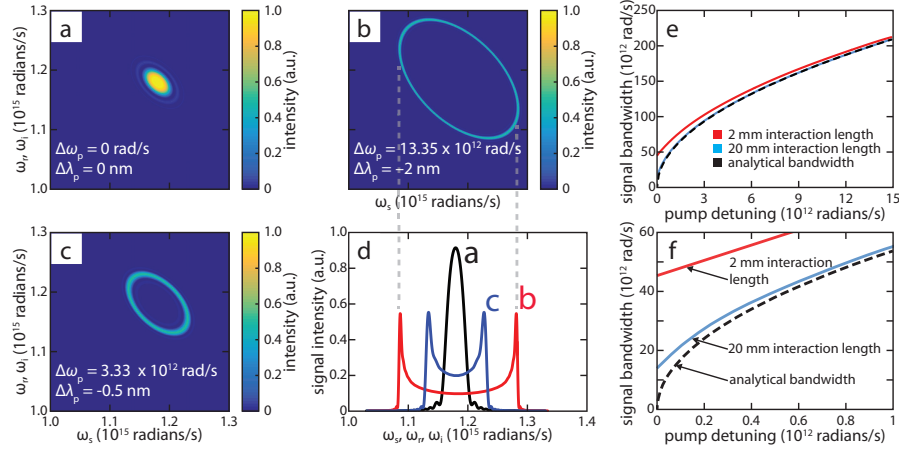


Fig. 2. We visualize the joint spectral intensity as an intensity plot of frequency versus frequency for several values of the pump detuning $\Delta\lambda_p$ from the PPM wavelength. Panels (a), (b) and (c) correspond to $\Delta_p = 0$, $\Delta_p = -2$ nm and $\Delta_p = -0.5$ nm, respectively. We assume a waveguide length $L = 2$ mm and use dispersion values for the phase matching point shown in Fig. 1(a). Fixing one of the three signal wavelengths (ω_s) on the horizontal axis, the two other signal wavelengths (ω_r and ω_i) are given by the two values on the vertical axis that intersect the ellipse. Phase matching is achieved along the perimeter of the ellipse and the thickness is determined by the pump and signal interaction length, based on Eq. (1). By collapsing the plots in (a), (b), and (c) onto the horizontal axis, we generate the spectra shown in (d). All three spectra are normalized by the total conversion efficiency. Panel (e) shows signal spectrum bandwidth as a function of pump detuning $\Delta\omega_p$. The dashed black curve gives the bandwidth defined by Eq. (2). Red and blue curves are numerically obtained signal bandwidths for waveguide lengths $L = 2$ mm and $L = 20$ mm, respectively. Panel (f) zooms near the PPM point.

is fulfilled for TOSPD as the signal bandwidth δ_s (derived in Appendix A), given by:

$$\delta_s = 2 \left(\frac{2}{3} \right)^{1/2} \left[\frac{2(v_p^{-1} - v_s^{-1})}{D_s} \Delta_p + \left(\frac{D_p}{D_s} \right) \Delta_p^2 \right]^{1/2}, \quad (2)$$

where $\Delta_p = \omega_p - \omega_p^0$ and $\Delta_m = \omega_m - \omega_p^0/3$, with $m = \{s, r, i\}$, are the pump and signal detunings from the PPM point. ω_p^0 is the pump frequency that gives PPM. v_p and v_s are the group velocities of the pump and signal modes at the PPM point, and D_p and D_s are their group velocity dispersion.

For a long interaction length L and a monochromatic pump with detuning Δ_p , the signal frequencies that satisfy energy and momentum conservation simultaneously can be represented in a (ω_s, ω_r) -plane by the ellipse (derived in Appendix A):

$$\Delta_s^2 + \Delta_r^2 - \Delta_r \Delta_s - \Delta_p (\Delta_r + \Delta_s) = A_p, \quad (3)$$

where $A_p = (3/16)\delta_s^2 - \Delta_p^2$. In Figs. 2(b) and 2(c), we plot the relative intensity of emitted signal photons in a frequency-frequency plane for cases where the pump is slightly detuned from the PPM point. The highest intensities occur at frequencies satisfying the ellipse equation above. The photon triplet wavefunction has a non-vanishing amplitude for signal frequencies outside

the ellipse in Eq. (3); however these frequencies are strongly suppressed because of poor phase matching (Figs. 2(b) and 2(c)).

The ellipse width δ_s grows with a scaling $(\Delta_p)^{1/2}$ for pump detuning $0 < \Delta_p < \Delta_p^c = 2(v_s - v_p)/(v_p v_s D_p)$ and with a scaling $(\Delta_p)^1$ for greater pump detuning. Maximizing signal D_s and minimizing $v_s - v_p$ and D_p minimizes signal bandwidth for finite phase mismatch. This provides a method to minimize signal bandwidth in the case that fabrication variations introduce finite phase mismatch. For fixed pump detuning Δ_p , the signal bandwidth δ_s in Eq. (2) corresponds to the distance between the highest and lowest points in the ellipse. The corresponding spectrum consists of a two-peak structure with intensity maxima occurring roughly at frequencies $\omega_p^0/3 \pm \delta_s/2$ (Fig. 2(d)). The spectra in Fig. 2 are obtained numerically by computing the triplet generation rate from Eq. (6) in Section 2.3.

In Fig. 2(e), we plot the signal bandwidth δ_s as a function of pump detuning Δ_p for the TiO₂ waveguide parameters from Fig. 1. The bandwidth is obtained from numerical spectra (as in Figs. 2a, b, and c) computed at 1/10-th the peak maximum, for the interaction lengths $L = 2$ mm and $L = 20$ mm. As the pump-signal interaction length increases, the spectral amplitude of the three-photon state (Section 2.3) approaches a delta function in the phase mismatch $\Delta k = k_p - k_r - k_s - k_i$. In this limit, the bandwidth δ_s in Eq. (2) accurately matches the numerical bandwidth. The discrepancy between analytical and numerically calculated bandwidth is greatest at $\Delta_p = 0$, with a minimum bandwidth $\delta_s = 54 \times 10^{12}$ rad/s for $L = 2$ mm and $\delta_s = 14 \times 10^{12}$ rad/s for $L = 20$ mm. As we discuss in Section 2.3, photon loss due to scattering and absorption reduces the effective interaction length, thus broadening the signal.

2.2. Effective nonlinearity and modal overlap

Once phase matching and energy conservation are satisfied for the interacting pump and signal modes, the efficiency of TOSPD is determined by the effective nonlinearity [24]:

$$\gamma = \frac{3\chi^{(3)}\omega_p}{4\epsilon_0 c^2 n^2} \eta, \quad (4)$$

where n is the material index and $\chi^{(3)}$ is the effective third-order susceptibility at the pump frequency. We can define η as the sum of mode overlap components $\eta_{ijkl} \equiv [A_{\text{eff}}^{ijkl}]^{-1} = \iint E_p^{i*} E_s^j E_s^k E_s^l dx dy$ between pump and signal electric field components [24] corresponding to all non-zero susceptibility tensor elements $\chi_{ijkl}^{(3)}$. The electric fields in this calculation are normalized. The non-zero tensor elements are determined by the material crystal structure and orientation.

Our TiO₂ is deposited on a thick thermal oxide and is thus polycrystalline with randomly oriented grains of diameter smaller than 50 nm. The lack of long-range order and the small grain size allows us to treat the material as effectively isotropic. Using the methods above we typically find an effective interaction area A_{eff} on the order of 10^{-10} m² for our TiO₂ waveguides. The details on how to obtain the nonlinear overlaps η_{ijkl} are given in Appendix B.

We calculate the effective nonlinearity γ in Eq. (4) for a pump and signal mode pair using mode profiles calculated with a commercial finite-difference eigenmode solver [29]. Because a significant part of the field in nanoscale waveguides is evanescent, we must consider the components of the mode profile that are in the waveguide core and cladding independently and utilize the corresponding nonlinear tensors.

Direct measurements of $\chi^{(3)}$ are difficult because of multi-photon absorption and other competing nonlinear interactions, especially at photon wavelengths below the half band gap;

therefore, we use the nonlinear index [30]

$$n_2 = \frac{3\chi^{(3)}}{4n_0^2\epsilon_0 c} \quad (5)$$

to parameterize the magnitude of the third-order nonlinearity. We use the value $n_2 = 4.65 \times 10^{-19} \text{ m}^2/\text{W}$ for the TiO_2 nonlinearity at 532 nm. This value is obtained from the bandgap scaling of $n_2(\lambda)$ [31] (see Appendix B for details).

2.3. Triplet generation rate in lossy waveguides

The rate of direct generation of photon triplets R_3 from TOSPD in the absence of photon losses has been calculated in previous work [16, 24]. Findings in Refs. [16, 24] can be qualitatively summarized by the expression $R_3 \approx \tilde{\zeta} N_p(0)L$, where $N_p(0)$ is the number of pump photons entering the waveguide and $\tilde{\zeta} \propto \gamma^2$ is the conversion efficiency per unit length, and L the waveguide length.

In the presence of photon losses, the triplet generation rate no longer increases linearly with L . We account for scattering losses by introducing pump and signal intensity attenuation coefficients α_p and α_s , respectively. We emphasize that an optimal length L_{opt} must exist such that the waveguide is long enough to generate a large number of triplets, but short enough so that a large fraction of complete triplets reaches the end when losses are taken into consideration. Extending the analysis in Ref. [24], we can express the triplet generation rate R_3 in the presence of losses for a continuous wave (cw) pump as (derivation in Appendix C)

$$R_3 = \frac{2^2 3^2 \hbar c^3 n_p^3}{\pi^2 [\omega_p^0]^2} \gamma^2 L^2 P \left(\frac{\omega_0}{n_0^2(\omega)} g(\omega_0) \right)^3 e^{-(\alpha_p + 3\alpha_s)L/2} \iint_{-\infty}^{\infty} d\nu_r d\nu_s |\Phi(\nu_r, \nu_s)|^2, \quad (6)$$

where the spectral amplitude $\Phi(\nu_r, \nu_s)$ is defined in Appendix C in terms of the frequency-dependent phase mismatch $\Delta k(\nu_r, \nu_s)$ and a loss mismatch parameter $\Delta\alpha = (\alpha_p - 3\alpha_s)$. P is the pump power and $\omega_0 = \omega_p^0/3$. The integration variables ν_r and ν_s are signal detunings from $\omega_p^0/3$.

We can compare the triplet generation rate from Eq. (6), which takes into account the dispersion properties of the signal mode around the phase matching point, with a simplified expression that ignores dispersion (derivation in Appendix C)

$$N_3 \equiv \int_0^L z \frac{dN_3(z)}{dz} = \tilde{\zeta} \frac{N_{p0}}{\alpha_p - 3\alpha_s} (e^{-3\alpha_s L} - e^{-\alpha_p L}), \quad (7)$$

where $\tilde{\zeta}$ quantifies the conversion efficiency. The device length that optimizes N_3 is thus given by $L_{\text{opt}} = [1/(\alpha_p - 3\alpha_s)] \ln(\alpha_p/3\alpha_s)$, for $\Delta\alpha = (\alpha_p - 3\alpha_s) \neq 0$.

In Fig. 3(a), we plot the normalized signal intensity in the waveguide as a function of the waveguide length L , for different amounts of photon loss in TiO_2 waveguides. The simplified model that ignores dispersion (Eq. (7)) is an excellent approximation for the results obtained by integrating the squared spectral amplitude $|\Phi(\nu_r, \nu_s)|^2$ (Eq. (6)) near points of PPM. In Fig. 3(b), we plot the optimal device length L_{opt} , as a function of the pump and signal loss parameters α_p and α_s . Highlighted is the parameter region for the waveguides considered in this work.

3. Device optimization

For efficient device operation, we maximize the triplet generation rate R_3 in Eq. (6). Given an optimal device length L_{opt} , we must thus minimize the phase mismatch Δk for the desired combination of pump and signal frequencies. This will produce narrow-bandwidth photon

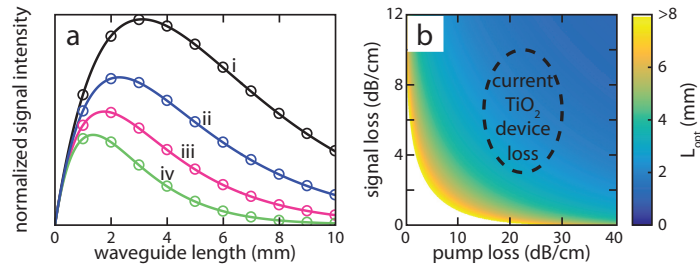


Fig. 3. (a) Signal intensity as a function of device length for pump and signal loss values, respectively, of (i) 16 and 4 dB/cm, (ii) 16 and 12 dB/cm, (iii) 28 and 4 dB/cm, and (iv) 28 and 12 dB/cm, representing losses on the lower and upper extremes for TiO₂ devices. Circles show the full quantum prediction, including signal dispersion, from Eq. (6) and lines show the prediction from Eq. (7). All curves are normalized by the maximum signal. (b) Ideal waveguide length plotted as a function of pump and signal losses. Current polycrystalline anatase TiO₂ waveguide losses give optimal device lengths $L_{\text{opt}} = 1 - 4$ mm. White denotes $L_{\text{opt}} > 8$ mm.

triplets as shown in Fig. 2(a) and 2(d). We must also maximize the effective nonlinearity γ by choosing a waveguide geometry that enhances the electric field overlap between pump and signal modes within a material with a high $\chi^{(3)}$ coefficient. We design TiO₂ waveguides with rectangular core geometry that achieve $\gamma = 1100 \text{ W}^{-1}\text{km}^{-1}$ while maintaining single mode operation at 1596 nm. In Section 3.1 we describe the optimization protocol used and in Section 3.2 we verify the design method with a demonstration of THG.

3.1. Optimization protocol

We design our devices for $\lambda_p = 532$ nm because high-power pump lasers with narrow bandwidth, high stability, and low cost are readily available at this wavelength. Our design protocol can be extended to other wavelengths and material platforms depending on the desired signal photon wavelength and available pump laser wavelength. Designing for a particular pump wavelength requires precise control of the waveguide dimensions [22,32,33].

We illustrate in Fig. 1(b) the geometry of our TiO₂ waveguides. The design parameters that can be tuned include: the waveguide core material, bottom cladding or substrate material, top cladding material, waveguide width, waveguide height, etch fraction, and the waveguide sidewall angle (θ). Due to the current state of the art in TiO₂ waveguide fabrication, we focus on fully etched, symmetric waveguide geometries with 90° sidewall angles.

We use a commercial finite-difference eigenmode solver [29] to complete our device design and optimization. For a given device geometry, we calculate all propagating modes and their dispersion properties at λ_p and $3\lambda_p$, using measured materials properties. We then use calculated mode dispersion properties to calculate the phase mismatch Δk for all mode pairs consisting of visible pump and IR signal. The mode profiles and the $\chi^{(3)}$ nonlinearity of the core and cladding materials are used to calculate the mode overlap and γ for all mode pairs (see Appendix B). This process is repeated for all device geometries to minimize phase mismatch and maximize γ .

We complete a sweep for rectangular waveguides, varying the waveguide height in the range 200 – 400 nm and width in the range 400 – 600 nm. This range of dimensions is chosen to ensure single mode operation at $3\lambda_p$, meaning only one TE and one TM guiding mode are supported by the waveguide. To quickly assess different waveguide geometries we introduce a

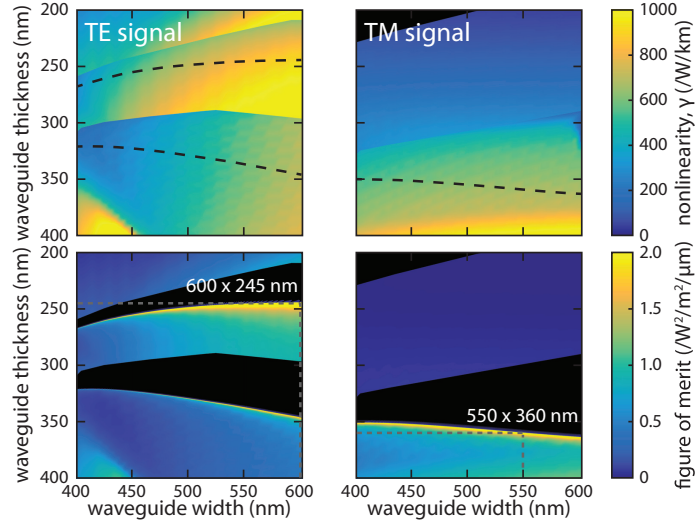


Fig. 4. (top) The effective nonlinearity γ as a function of waveguide width and thickness for the best phase-matching point. The highest $\gamma = 1100 \text{ W}^{-1}\text{km}^{-1}$ is achieved in a $600 \times 300 \text{ nm}$ waveguide for TE signal and a $600 \times 400 \text{ nm}$ waveguide for TM signal. However, these dimensions do not achieve phase-matching. Lines mark regions with high \mathcal{F} which do achieve phase-matching. (bottom) Figure of merit \mathcal{F} as a function of waveguide dimensions. The best combination of phase matching and γ are achieved at $600 \times 245 \text{ nm}$ ($\gamma = 908 \text{ W}^{-1}\text{km}^{-1}$) for TE signal and $550 \times 360 \text{ nm}$ ($\gamma = 674 \text{ W}^{-1}\text{km}^{-1}$) for TM signal.

figure of merit that describes the effective spectral density of signal photons

$$\mathcal{F} = \frac{\gamma^2}{\delta_s}, \quad (8)$$

where the minimum signal bandwidth $\min\{\delta_s\} = \Delta_{\text{PPM}}$ is given by the PPM bandwidth in Eq. (1) for degenerate TOSPPDC. For each set of waveguide dimensions, we find the mode pair (pump and signal) with the lowest phase mismatch that has non-zero effective nonlinearity. In Fig. 4, we show the effective nonlinearity γ and figure of merit \mathcal{F} for the best phase matched mode pair with the fundamental IR signal mode, as a function of waveguide dimensions. Regions that are colored in black for the TM signal γ do not support a TM signal mode. Discontinuities in the plots of γ arise when the pump mode with the lowest phase mismatch changes. The regions with high \mathcal{F} in Fig. 4 are further restricted by the fact that the conversion efficiency drops significantly for negative phase mismatch $\Delta k < 0$ (black regions) because normal dispersion in the signal modes at the signal frequencies makes simultaneous phase matching and energy conservation impossible. Rapid broadening of the signal spectrum when shifting waveguide dimensions away from regions that achieve PPM greatly reduces \mathcal{F} .

We extract the optimal waveguide dimensions using the maximum values of \mathcal{F} (Table 1). Choosing a region where a high figure of merit is maintained for a larger range of waveguide dimensions can reduce the negative impacts of fabrication tolerances on device performance in experimental demonstrations. The same figure of merit can be used to optimize other waveguide parameters and geometries.

Table 1. Waveguide Parameters for Phase-matching Regions With High Figure of Merit \mathcal{F} . \mathbf{e}_s is the Signal Mode Polarization and γ the Effective Nonlinearity.

\mathbf{e}_s	Width (nm)	Thickness (nm)	γ ($\text{W}^{-1}\text{km}^{-1}$)	Δ_{PPM} (μm)	\mathcal{F} ($\text{W}^{-2}\text{m}^{-2}\mu\text{m}^{-1}$)
TE	400 – 600	268 – 245	291 – 908	0.046 – 0.051	1.81 – 16.2
TE	400 – 600	322 – 346	233 – 718	0.044 – 0.062	1.22 – 11.6
TM	400 – 600	351 – 364	522 – 671	0.044 – 0.048	6.19 – 14.0

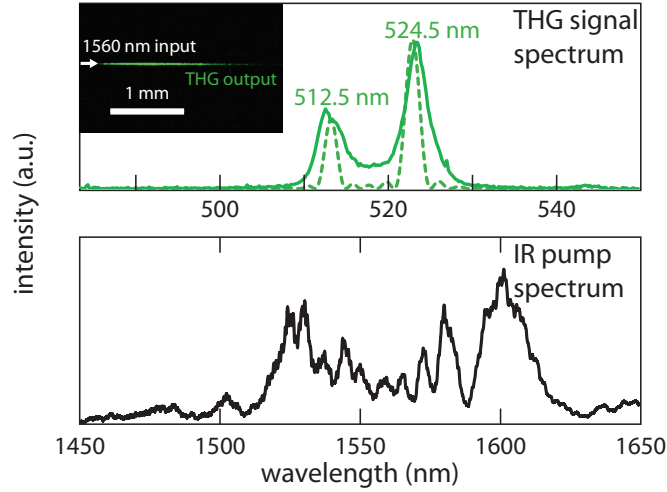


Fig. 5. Experimental demonstration of THG in an integrated waveguide with two phase-matching points within the infrared pump bandwidth (black curve). The calculated THG signal (dashed curve) shows agreement with the measured THG signal (solid green curve). The inset shows a top-down image of scattered THG signal from the waveguide.

3.2. Experimental validation of the protocol

The reverse process of TOSPD, THG, has been demonstrated in nanoscale polycrystalline anatase TiO_2 waveguides by Evans *et al.* [22]. Because the same energy conservation, phase matching and mode overlap constraints govern both processes, we perform similar experimental validation of our design methods by means of THG measurements.

The waveguide (780×244 nm) is designed to have multiple phase-match points within the TE-polarized pump bandwidth. Using the techniques from Sections 2.1 and 2.2, we calculate phase match points with $\gamma = 253$ and $304 \text{ W}^{-1}\text{km}^{-1}$ at 513.3 and 523.0 nm, respectively. In Fig. 5, we plot the expected relative intensities of THG based on the measured input pump spectrum, calculated mode dispersion, and calculated γ of both mode pairs, showing close agreement with experimental results. The experimental phase-match points are within 1.5 nm of the calculated phase match points and the measured THG signal is broader by approximately 3 nm. This can be explained by variations in waveguide width of ± 5 nm and thickness of ± 2 nm along the length of the waveguide. These variations are within the measured fabrication tolerances of waveguide width and roughness of the film used to fabricate the device. This demonstration experimentally shows that the device design methods outlined in this paper can be used to optimize devices for THG and, consequently, TOSPD.

3.3. Realistic device performance

Combining the results of the design sweeps presented in Figs. 3 and 4 with measured losses, we estimate TOSPD device performance. We have previously measured losses as low as 4 dB/cm in polycrystalline anatase TiO₂ waveguides in the telecommunications wavelengths [20, 26] and estimate losses of 20–30 dB/cm at 532 nm. With this amount of losses, the optimal device length is $L_{\text{opt}} = 2.2 - 2.8$ mm. We estimate a photon triplet conversion efficiency of 0.1 – 0.13 triplets/s/mW of pump power and maximum generation rate of 130 – 160 triplets/s. This rate takes into account an optimal end-fire coupling efficiency of 20.6% calculated for the 550×360 nm waveguide and higher-order pump mode described in Fig. 1 and an input pump power of 1250 mW at 532 nm, corresponding to the measured damage threshold of our TiO₂ devices. We note that the TE signal phase-matching point in a 600×245 nm waveguide does have a higher γ , however, the photon triplet generation rate would be lower due to a maximum end-fire coupling efficiency of only 10.5% into the higher-order pump mode. We use a nonlinear index of $n_2 = 4.65 \times 10^{-19}$ m²/W. Film losses as low as 3 dB/cm in the telecommunications wavelengths and 15 dB/cm in the visible wavelengths have been measured using prism coupling techniques [20]. By optimizing the fabrication, we can reduce losses to the limit of the film losses, increasing the optimal device length to 3.7 mm and the maximum triplet generation efficiency to 0.17 triplets/s/mW of pump power, over an order of magnitude higher than previous theoretical and experimental results [13, 14, 24, 25, 34]. This highlights the importance of reducing photon losses in waveguide-based devices.

4. Temporal coherence of TOSPD sources

Second-order spontaneous parametric down conversion (SPDC) generates photon pairs that possess quantum correlations in energy and time degrees of freedom. This energy-time entanglement can be exploited in quantum communication protocols [35, 36]. Our TOSPD sources are expected to exhibit tripartite energy-time entanglement. However, the type of encoding of quantum information that can be exploited for quantum communication protocols with our source ultimately depends on the spectral and temporal coherence properties of the down-converted signal [37]. In this section we therefore discuss the coherence properties of TOSPD sources for realistic detector and loss parameters.

The temporal coherence of a triplet source can be characterized in three-photon coincidence detection experiments, which gives access to the third-order intensity correlation function [16]

$$G^{(3)}(x_1, x_2, x_3) = \langle E^{(-)}(x_1)E^{(-)}(x_2)E^{(-)}(x_3)E^{(+)}(x_3)E^{(+)}(x_2)E^{(+)}(x_1) \rangle, \quad (9)$$

where $\hat{E}^{(+)}(x_j)$ is an operator describing the propagating electric field at the j -th detector, with $\hat{E}^{(-)} = [\hat{E}^{(+)}]^\dagger$. The field at the detector is given by a wavepacket of the form $\hat{E}^{(+)}(x_j) = \int d\omega f_j(\omega) \hat{a}(\omega) \exp[-i\omega x_j]$, where $\hat{a}(\omega)$ is a free-space bosonic operator. We assume a Gaussian detector filter function $f_j(\omega) = f_0 \exp[-(\omega - \omega_j)^2 / 2\sigma_j^2]$ [8]. f_0 is a normalization constant and ω_j is the center frequency of the j -th spectral filter. For simplicity, we assume that all filters have the same bandwidth $\sigma_k = \sigma$.

The $G^{(3)}(x_1, x_2, x_3)$ correlation function is proportional to the probability of detecting a photon at the space-time location $x_1 = t_1 - r_1/c$, followed by a detection event at location $x_2 = t_2 - r_2/c$ and another one at $x_3 = t_3 - r_3/c$. In this notation, the j -th detector fires at time t_j at a distance r_j from the TOSPD output. This triple coincidence signal can be computed for an output triplet state $|\Psi_3\rangle$ as

$$G^{(3)}(x_1, x_2, x_3) = |\langle 0 | E^{(+)}(x_3)E^{(+)}(x_2)E^{(+)}(x_1) | \Psi_3 \rangle|^2. \quad (10)$$

We are interested in $G^{(3)}$ for a triplet state generated by a narrow band cw pump near the perfect phase matching point (PPM), defined in Section 2.1. For a pump photon with fixed frequency

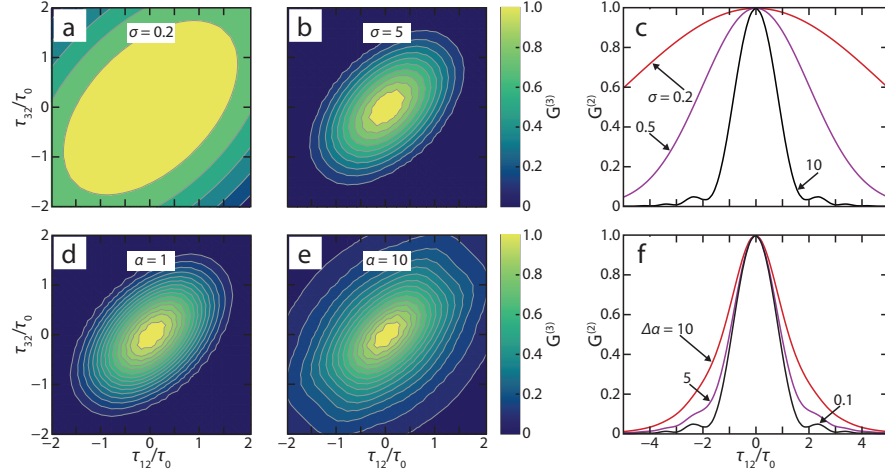


Fig. 6. Triple and two-photon coincidence signals for detectors placed at equal distances from the TOSPD output. Time delays $\tau_{12} = t_1 - t_2$ and $\tau_{32} = t_3 - t_2$ are given in units of the characteristic timescale $\tau_0 = \sqrt{D_s L}/2$. Panels (a) and (b) are $G^{(3)}$ functions for the detector filter bandwidths $\sigma = 0.2\nu_0$ and $\sigma = 5\nu_0$, respectively, with a loss mismatch parameter $\Delta\alpha L \equiv (\alpha_p - 3\alpha_s)L = 0.1$. Panels (d) and (e) correspond to the $G^{(3)}$ functions for $\Delta\alpha L = 1$ and $\Delta\alpha L = 10$, respectively, with a detector bandwidth $\sigma = 5\nu_0$. Panel (c) is the $G^{(2)}$ function for several values of σ with fixed $\Delta\alpha L = 0.1$ and (f) is the $G^{(2)}$ signal for several values of $\Delta\alpha L$ with fixed $\sigma = 5\nu_0$. Frequency is in units of $\nu_0 = 1/\tau_0$, L is the waveguide length and D_s is the group velocity dispersion (GVD) of the signal guiding mode. Plots are normalized to their maximum values.

ω_p^0 and wavenumber k_p^0 , the triplet state $|\Psi_3\rangle$ is a continuous wavepacket describing three signal photons having frequencies $(\omega_r, \omega_s, \omega_t)$ that satisfy energy and momentum conservation. The triplet wavepacket is characterized by a joint spectral amplitude function $\Phi(\omega_r, \omega_s, \omega_t)$, whose imaginary part depends on the amount of pump and signal losses. We refer the reader to Appendix C for more details on this point. Signal photon frequencies that are detuned from the PPM point, lead to a phase mismatch $\Delta k \neq 0$. For the triplet state $|\Psi_3\rangle$ described in Appendix C, we numerically evaluate the $G^{(3)}$ function by expanding the frequency mismatch Δk up to second order in signal detunings from PPM.

In Fig. 6 we plot the computed $G^{(3)}$ signals with time delays in units of the timescale $\tau_0 = \sqrt{D_s L}/2$, where L is the waveguide length and D_s is the group velocity dispersion (GVD) of the signal guiding mode. For a typical optimized TiO_2 waveguide with $L = 2$ mm and $D_s = 5.36 \times 10^{-3}$ ps²/mm, the characteristic coherence time is $\tau_0 = 73$ fs. The signal depends on the bandwidth σ of the detectors, given here in units of $1/\tau_0$, as well as the loss mismatch parameter $\Delta\alpha \equiv (\alpha_p - 3\alpha_s)$, which characterizes the frequency-time decoherence of the triphoton state. For our 2 mm long waveguides, we have a small loss mismatch $\Delta\alpha L \approx 0.08$. The mirror symmetry around $\tau_{12} = \tau_{32}$ is due to the fact that all photons in a triplet have the same GVD in mode-degenerate TOSPD. The FWHM of the $G^{(3)}$ function along the cut $\tau_{12} = -\tau_{32}$ is roughly equals to τ_0 for large detector bandwidths $\sigma\tau_0 \gg 1$. Small bandwidths $\sigma\tau_0 \ll 1$ broaden the $G^{(3)}$ function such that highly correlated photons can be detected within a wide range of time delays. This behaviour resembles the two-photon coincidence signals for second-order SPDC sources [8]. Increasing the loss mismatch $\Delta\alpha$ also broadens the $G^{(3)}$ function, but in a qualitatively different way. Photon losses directly broaden the joint

spectral amplitude $\Phi(\omega_r, \omega_s, \omega_i)$, which characterizes the wavepacket structure of the triplet state $|\Psi_3\rangle$ in the frequency domain. This broadening is independent of the time-domain field representation of $|\Psi_3\rangle$ at the detectors, the so-called triphoton wavepacket $\psi(x_1, x_2, x_3) \equiv \langle 0|E^{(+)}(x_3)E^{(+)}(x_2)E^{(+)}(x_1)|\Psi_3\rangle$, which involves shaping the triplet state $|\Psi_3\rangle$ by the detector filters.

We finally consider a scenario where only two photons of the TOSPD source are detected in coincidence measurements. In other words, we discard the information about the third photon. The resulting coincidence signal is proportional to the correlation function $G^{(2)}(x_1, x_2)$, the second order analogue of $G^{(3)}$. For the TOSPD triplet state $|\Psi_3\rangle$, this signal can be written as

$$G^{(2)}(x_1, x_2) = \int d\omega_3 |\langle 0|a(\omega_3)E^{(+)}(x_2)E^{(+)}(x_1)|\Psi_3\rangle|^2. \quad (11)$$

We compute the $G^{(2)}$ correlation function as described in Appendix D for a source pumped at the PPM point, for several values of the detector bandwidth σ and loss mismatch $\Delta\alpha$. The results are shown in Fig. 6 (panels c and f). The two-photon correlation function has qualitatively the same behaviour as the $G^{(3)}$ function with σ and $\Delta\alpha$. Its width is also on the order of $1/\tau_0$ for $\sigma\tau_0 \gg 1$. These results show that unlike an SPDC process, where detection of one photon in a photon pair destroys any useful entanglement [8], frequency-time entanglement in a TOSPD source is robust against single photon losses [38].

5. Conclusion and outlook

We provide design principles for practical on-chip sources of photon triplets generated via TOSPD and discuss the non-unitary propagation of the photon triplet state in the presence of pump and signal photon losses. Including the impact of losses is critical, especially when operating at visible wavelengths where surface roughness and fabrication imperfections are closer to the size of a single wavelength and material absorption increases close to the band edge of the waveguide core material. The design methods discussed in this work can be applied broadly to various device geometries, loss conditions, and material platforms. This will facilitate experimental demonstrations of spontaneously generated photon triplets and development of a platform for commercially viable sources.

We use TiO_2 to illustrate our design protocol. TiO_2 is a promising material platform for an integrated entangled photon triplet source due to its transparency across the visible and telecommunication wavelengths as well as its high linear and nonlinear refractive indices. We discuss the mean signal flux and prospects for detecting continuous-variable entanglement of the photon triplet quantum state in the presence of photon loss. We calculate triplet generation rates on the order of 10^{-1} triplets/s/mW of pump power, which exceeds the triplet generation efficiencies obtained by cascading entangled photon pairs by an order of magnitude. Our work thus sets the stage for the development of on-chip photon triplet sources for applications in photonic quantum technologies.

Improvements to the proposed waveguide design and current fabrication techniques can greatly enhance generation rates and accelerate experimental efforts. Generating photon triplets within an integrated micro-ring resonator or resonant cavity can provide an additional constraint on the spectrum of generated photons, enabling greater spectral control of the output signal via the Purcell effect. Optimization of fabrication processes, including resist reflow techniques and new etchless fabrication techniques [39], can reduce waveguide losses. Photonic crystals and slot waveguides can be used to greatly enhance the effective nonlinearity of integrated photonic devices [40].

Device performance can also benefit from improvements in material deposition. Film optimization through epitaxial growth has the potential to dramatically reduce scattering losses

due to grain boundaries, increasing the achievable optimal device length and conversion efficiency. Rutile TiO₂ is unexplored as a photonic device platform although other studies have shown extraordinarily high nonlinearity at visible wavelengths in this material [41]. Alternatively, exploring other material platforms, for example silicon nitride or diamond, may enable better devices despite their lower nonlinearity due to the trade-offs between propagation losses, nonlinearity, and damage threshold.

Several experimental considerations need to be taken into account for successful measurements of photon triplets. Although a pulsed pump would enable gated detection schemes important for many applications, competing intensity-dependent nonlinear interactions, such as multi-photon absorption and self- and cross-phase modulation, would limit the usable pulse energy and attainable photon triplet generation rate. Secondly, spectral filtering at the device output is necessary to reduce noise from residual pump photons. Lastly, as in all experimental demonstrations, the rate of detected photon triplets is lower than the generated rate due to losses at the device output, detector efficiency, and the detection scheme for measuring 3-photon coincidences. These factors, coupled with the required fabrication precision for realizing an efficient device, highlight the challenges associated with an experimental demonstration.

In summary, we have developed a design protocol to optimize the efficiency of TOSPDG in nanoscale waveguides. We illustrate the scheme using TiO₂ photonic chips, but the method is general and can be applied to any material platform. Entangled photon triplets generated this way can find applications in quantum tasks that can benefit from states with non-Gaussian quantum statistics, serve as a starting point to build large entangled states of light for quantum information purposes, or to develop novel spectroscopic tools.

A. Signal bandwidth for mode-degenerate TOSPDG

In this Appendix we derive Eq. (2) of the main manuscript, for the signal bandwidth Δ_s . We expand the signal and pump wavenumbers around the perfect phase-matching (PPM) point. We allow the signal and pump frequencies to be detuned from this crossing by the quantities $\Delta_m = \omega_m - \omega_p^0/3$ with $m = \{s, r, i\}$. The phase-matching condition at the PPM point reads $k_p^0 = 3k_s^0$. Expanding the pump and signal wavenumbers around PPM with respect to the pump and signal detunings, the condition $(k_p - k_s - k_r - k_i) = 0$ yields

$$(\Delta_s^2 + \Delta_r^2 + \Delta_i^2) = \frac{2(v_p^{-1} - v_s^{-1})}{D_s} \Delta_p + \left(\frac{D_p}{D_s}\right) \Delta_p^2 \equiv r_p^2 \quad (12)$$

where $v_m \equiv d\omega_m/dk_p$ and $D_m \equiv d^2k_m/d\omega_m^2$ are the mode group velocity and group velocity dispersion (GVD) of the m -th photon at the PPM point. Because the three signal photons belong to the same guided mode, they have the same values of v_s and D_s , defined at $\omega_p^0/3$.

We use energy conservation to simplify the linear terms with respect to the signal detunings. Eq. (12) shows that for mode-degenerate and frequency non-degenerate TOSPDG, phase matching can be satisfied by the signal detunings Δ_m that lie on the surface of a sphere with radius r_p , subject to the linear constraint $\Delta_p = \Delta_s + \Delta_r + \Delta_i$, due to energy conservation. We define dimensionless signal detunings $x_m = \Delta_m/\Delta_p$, for $m = \{r, s\}$, and the parameter $a_p = r_p^2/(2\Delta_p^2) - 1$ (in Eq. 3 we use $A_p = a_p\Delta_p^2$). The points satisfying both energy and momentum conservation form the ellipse

$$x_s^2 + x_r^2 - x_r x_s - x_r - x_s = a_p. \quad (13)$$

The signal bandwidth is therefore given by the distance between the critical points $x_s = 1 \pm \sqrt{(1+a_p)/3}$. Inserting the expression for a_p and inserting the original frequency variables we

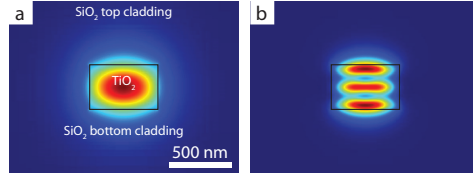


Fig. 7. Examples of (a) a signal mode power density profile and (b) pump mode power density profile. These mode profiles are for a TM_{00} signal mode and TM_{02} pump mode phase matched at 532 nm in a 550×360 nm TiO_2 waveguide with SiO_2 cladding (first presented in Fig. 1 of the main text).

can write the signal bandwidth as

$$\delta_s \equiv \sqrt{\frac{2}{3}} \times 2r_p = 2 \left(\frac{2}{3} \right)^{1/2} \left[\frac{2(v_p^{-1} - v_s^{-1})}{D_s} \Delta_p + \left(\frac{D_p}{D_s} \right) \Delta_p^2 \right]^{1/2}, \quad (14)$$

which exhibits a crossover in the scaling $(\Delta_p)^\alpha$ from $\alpha = 1/2$ to $\alpha = 1$ roughly at the pump detuning $|\Delta_p| = 2|v_s - v_p|/(v_s v_p D_p)$.

B. Overlap calculation with nonlinear susceptibility tensor elements

In this Appendix, we provide a generalized method of calculating overlap η and effective nonlinearity γ that can be applied to any crystal symmetry and orientation, as well as a derivation of the symmetry conditions that apply in polycrystalline anatase TiO_2 . We calculate the effective nonlinearity of TOSPDG for phase-matched pump and signal modes using the definition

$$\gamma = \frac{3\chi^{(3)}\omega_p}{4\epsilon_0 c^2 n^2} \eta, \quad (15)$$

where n is the material index, $\chi^{(3)}$ is the nonlinear susceptibility and η is the overlap between the modes. Crystal symmetry is taken into account to determine relative magnitudes of $\chi^{(3)}$ tensor elements. We discuss considerations relevant to determining the strength of the nonlinearity at the pump wavelength.

The overlap between phase-matched pump and signal modes propagating along the z -direction is calculated using the x, y, z electric field components of each mode as

$$\eta_{ijkl} = \frac{\iint dx dy E_p^{i*} E_s^j E_s^k E_s^l}{\left[\iint |E_p(x, y)|^2 dx dy \right]^{1/2} \left[\iint |E_s(x, y)|^2 dx dy \right]^{3/2}}, \quad (16)$$

where $E_p^i(x, y)$ and $E_s^j(x, y)$ are the components of the pump and signal mode electric fields. The denominator in Eq. (16) normalizes the pump and signal fields such that they satisfy the condition $\iint |E|^2 dx dy = 1$. Figure 7 gives an example of a pair of modes with non-zero overlap.

Spatial distributions of the x, y, z E -field components of each mode in Eq. (16) are calculated using simulations [29]. The subscripts i, j, k, l correspond to the Cartesian indices for crystal axes along which the E -field is polarized. In our notation, the first index refers to the pump polarization and the subsequent three indices refer to the polarization of the signal modes. In the degenerate TOSPDG case, all three signal modes have the same E -field distribution.

To illustrate the calculation of overlap terms for a specific $\chi^{(3)}$ tensor element, we first consider the simplest case of an E -field and a single crystal oriented along the same axes

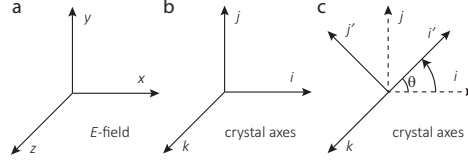


Fig. 8. Examples of a) E -field orientation, b) crystal axes orientation and c) crystal axes orientation with a rotation by an arbitrary angle in the xy plane.

(Figs. 8(a) and 8(b)). We use indices x, y, z for the E -field coordinate axes and i, j, k, l for the crystal axes. In this case, the χ_{ijjj} contribution to the TOSPD process is determined by the field overlap component $\eta_{ijjj} = \iint E_p^{x*} E_s^x E_s^y E_s^y dx dy$. For the same electric field orientation but a different crystal orientation shown in Fig. 8(c), the contribution of the χ_{ijjj} term is calculated by projecting the E -field onto the crystal axes, such that *e.g.* $E_i = E_x \cos \theta + E_y \sin \theta$ and $E_j = -E_x \sin \theta + E_y \cos \theta$ and $E_k = E_z$, and then computing $\eta_{ijjj} = \iint E_p^{i*} E_s^i E_s^j E_s^j dx dy$. Because the crystal symmetry determines the nonlinearity, projecting the E -field onto the crystal axes allows us to calculate the total nonlinear overlap with the fewest number of unique terms, η_{ijkl} .

There are 81 possible permutations of the field polarizations in the overlap calculation for η_{ijkl} . Their contribution to the total overlap is determined by the magnitude of the corresponding nonlinear susceptibility tensor element, χ_{ijkl} . The material crystal structure of the waveguide determines which χ_{ijkl} terms are non-zero and their relative magnitudes. As an example, anatase TiO_2 has tetragonal symmetry and belongs to the crystal class $4/mmm$. Our anatase TiO_2 films polycrystalline with randomly oriented grains much smaller than the wavelength ($\lambda_s/30$ and $\lambda_p/10$). As a result, an incoming field along the x -direction polarizes the medium along all orthogonal crystal axes. Furthermore, this response is indistinguishable from the polarization of the medium when the incoming field is along y or z . Therefore, we can treat the material as effectively isotropic. The relationships between non-zero isotropic tensor elements can be found in Ref. [30] and are as follows:

$$\begin{aligned} j j k k = k k j j = k k i i = i i k k = i i j j = j j i i ; j k k j = k j j k = k i i k = i k k i = i j j i = j i i j \\ j k j k = k j k j = k i k i = i k i k = i j i j = j i j i ; i i i i = j j j j = k k k k = i i j j + i j j i + i j j i \end{aligned} \quad (17)$$

For a material containing large grains with n crystal orientations, the E -field projection can be performed on each of the n crystal axes to identify the overlap terms of interest for each non-zero $\chi^{(3)}$ term. Considering the small grain sizes and the assumption of isotropic crystal symmetry in our waveguide medium, we can significantly simplify this process. The relations in Eq. (17) show that there are three independent $\chi^{(3)}$ variables: $i i j j$, $i j i j$ and $i j j i$. Furthermore, when we consider the degenerate TOSPD case, we find that all three signal modes are the same; therefore, with a given pump index, we can arbitrarily arrange the signal indices and obtain the same overlap:

$$\eta_{i i j j} = \eta_{i j i j} = \eta_{i j j i}. \quad (18)$$

This leads to three important conclusions: (i) all overlap terms of interest can be calculated by considering a single crystal axis orientation; (ii) using the relations in Eq. (18) we can simplify the number of overlap terms we calculate from 21 to 9 unique terms; and, (iii) we find that $\chi_{i i i i} = \chi_{j j j j} = \chi_{k k k k} = 3\chi_{i i j j}$, meaning that the contribution of the diagonal nonlinear tensor elements $\chi_{i i i i}$, $\chi_{j j j j}$ and $\chi_{k k k k}$ is three times stronger than the contribution generated by the non-zero off-diagonal terms. Note that there are three times as many off-diagonal $\chi^{(3)}$ terms, so that each of the 9 unique overlap terms makes an equal contribution to the total overlap.

Based on the symmetry of the $\chi^{(3)}$ tensor, we can also gain an intuition for which combinations of mode profiles yield non-zero overlap and contribute to the effective nonlinearity. In the case of polycrystalline TiO₂, each of the x , y , and z components appears an even number of times in each non-zero $\chi^{(3)}$ tensor element. The mode profile of the x , y , and z components of the field must therefore be even, meaning that sign of E_x , E_y , and E_z is symmetrical about the x and y axes. Alternatively, an even number of odd field profiles must be present to yield non-zero overlap.

Nanoscale waveguides often have a significant evanescent field, requiring that nonlinear overlaps take into account different $\chi^{(3)}$ nonlinearities in the core and cladding regions. In this case, the integration in Eq. (16) is carried out over the area of the core, top cladding, and bottom cladding separately. These values are then used to calculate γ in each region separately using Eq. (15). The total effective nonlinearity of the waveguide will be the sum $\gamma = \gamma_{\text{core}} + \gamma_{\text{topcladding}} + \gamma_{\text{bottomcladding}}$.

In the main text we note that the $\chi^{(3)}$ nonlinearity is parametrized using the nonlinear index

$$n_2 = \frac{3\chi^{(3)}}{4n_0^2\epsilon_0 c}, \quad (19)$$

which is often measured using Z-scan and self-phase modulation techniques, both of which also rely on third-order nonlinear interactions. In order to produce photon triplets in the telecommunications band via TOSPD, the pump wavelength is in the visible. Z-scan and self-phase modulation measurements are challenging in the presence of two-photon absorption and other effects prevalent below the half-bandgap wavelength [41,42]. For this reason, we have applied a bandgap scaling approach of n_2 [31] to nonlinearities measured in polycrystalline anatase TiO₂ films for the range of wavelengths $\lambda = 800 - 1560$ nm [19]. The estimated value of n_2 can be considered as a lower bound because the model in Ref. [31] is known to underestimate the magnitude of the nonlinearity at photon energies above three-quarters of the bandgap. As a result, our calculated nonlinearities for a 532-nm pump wavelength and the corresponding photon triplet generation rates can be considered a lower bound on expected device performance.

In conclusion, we find the total overlap in polycrystalline anatase TiO₂ by summing 9 unique overlap terms calculated using Eq. (16). The effective nonlinearity is calculated, in turn, using the total overlap as an input parameter in Eq. (4) of the main text. Our approach for determining the effective interaction area and effective nonlinearity by assuming that our material has isotropic symmetry can be used for other polycrystalline materials with grains on the order of $\lambda/10$ or smaller. In addition, the general approach describes how to determine the effective nonlinearity for arbitrary crystal symmetries, crystal orientations and electric field orientations.

C. Triplet generation rate in presence of propagation losses

In this appendix we derive Eqs. (6) and (7) of the main text. We note that the effects of multiphoton absorption are ignored in this analysis and justify this assumption for the waveguide parameters presented in the main text.

We use a formalism that extends the approach in Refs. [16,24]. The starting point is the expression for the TOSPD light-matter interaction Hamiltonian

$$\hat{H}_I = \frac{3\epsilon_0\chi^{(3)}}{4} \int dV \hat{E}_p^{(+)}(\mathbf{r},t) \hat{E}_r^{(-)}(\mathbf{r},t) \hat{E}_s^{(-)}(\mathbf{r},t) \hat{E}_i^{(-)}(\mathbf{r},t) + \text{H.c.} \quad (20)$$

in terms of the electric field operators $\hat{E}^{(+)}(\mathbf{r},t) = iA(x,y)\sqrt{\delta k \sum_k \ell(\omega)} \exp[i(kz - \omega t)]\hat{a}(t)$, where $\ell(\omega) = \sqrt{\hbar\omega/\pi\epsilon_0 n^2(\omega)}$. ϵ_0 is the vacuum permittivity, $n(\omega)$ the refractive index, and \hbar

is Planck's constant. The label p refers to the pump field, and $\{r, s, i\}$ refer to the signal fields. $\delta k = 2\pi/L_Q$ is the mode spacing defined by the quantization length L_Q , $A(x, y)$ characterizes the transverse spatial distribution of the field, taken to be normalized and frequency-independent.

We describe the pump mode as a strong classical field of the form

$$E_p^{(+)}(\mathbf{r}, t) = A_0 A_p(x, y) \int d\omega_p \beta(\omega_p) e^{[i(k_p(\omega_p)z - \omega_p t)]}, \quad (21)$$

and consider the pump Gaussian amplitude $\beta(\omega_p) = 2^{1/4}/(\pi^{1/4}\sqrt{\sigma})\exp[-(\omega_p - \omega_p^0)^2/\sigma^2]$ where ω_p^0 is the pump carrier frequency and σ the pump pulse bandwidth. In general, A_0 is related to the peak pump power, but for a Gaussian pump amplitude, it is related to the average pump power P by $A_0 = \sqrt{P/\pi\epsilon_0 c n_p R}$, with R the pulse repetition rate and $n_p = n(\omega_p^0)$.

In the absence of propagation losses, first-order perturbation theory with respect to the interaction Hamiltonian allows us to write the output signal state as [8]

$$|\Psi\rangle = \left[1 - \frac{i}{\hbar} \int_{t_0}^t dt' H_I(t')\right] |0\rangle = |0\rangle + \lambda |\Psi_3\rangle. \quad (22)$$

The photon triplet state can be written as

$$|\Psi_3\rangle = \int d\omega_p \beta(\omega_p) \sum_{k_s, k_r, k_i} \ell(\omega_r) \ell(\omega_s) \ell(\omega_i) \left[\int_{t_0}^t dt' \int dz \phi(t, z) \hat{a}^\dagger(k_r) \hat{a}^\dagger(k_s) \hat{a}^\dagger(k_i) |0\rangle \right], \quad (23)$$

where $\omega_m = \omega(k_m)$ for $m = \{s, r, i\}$. We have defined the frequency-dependent function $\phi(t, z) = \exp[i\Delta\omega t] \exp[i\Delta k z]$, where $\Delta k = (k_p - k_r - k_s - k_i)$ is the phase mismatch and $\Delta\omega = (\omega_r + \omega_s + \omega_i - \omega_p)$ the energy mismatch. The spatial integration is carried out over the waveguide length L . The photon triplet state amplitude λ is given by

$$\lambda = \frac{3\epsilon_0 \chi^{(3)} A_0}{4\hbar A_{\text{eff}}} (\delta k)^{3/2}, \quad (24)$$

where the effective area is the inverse of η given in Eq. (16).

In order to include the propagation losses, we model them phenomenologically through an exponential decay of the pump and signal fields. This approach ignores the probability of observing signal modes with one or two photons as a result of photon scattering. Such conditional states are highly unlikely to occur because the signal modes are found in the vacuum $|0\rangle$ with a near unit probability because $\lambda \ll 1$. We are interested in the part of the output state that involves three photons. If the interaction takes place at position z within a waveguide that spans $z = [-L/2, L/2]$, the corresponding amplitude is decreased by a factor: $e^{-(\alpha_p/2)(z+L/2)} e^{-3(\alpha_s/2)(L/2-z)}$, where we have used the attenuation coefficients α_p and α_s (in units of inverse length) to describe pump and signal photon loss, respectively. Therefore, the photon triplet state in Eq. (23) needs to be modified in the presence of photon losses to read

$$\begin{aligned} |\Psi_3\rangle &= \int d\omega_p \beta(\omega_p) \sum_{k_r, k_s, k_i} \ell(\omega_r) \ell(\omega_s) \ell(\omega_i) \\ &\times \left[\int_{t_0}^t dt' \int dz \phi(t', z) e^{-(\alpha_p - 3\alpha_s)z/2} e^{-(\alpha_p + 3\alpha_s)L/4} \times \hat{a}^\dagger(k_r) \hat{a}^\dagger(k_s) \hat{a}^\dagger(k_i) |0\rangle \right]. \end{aligned} \quad (25)$$

Because the propagation times inside the waveguide are much longer than $1/\Delta\omega$, we carry out the time integration by setting $t_0 = -\infty$ and $t = \infty$ and obtain the energy conservation rule $\int_{-\infty}^{\infty} dt' \phi(z, t) = 2\pi e^{i\Delta k z} \delta(\omega_p - \omega_r - \omega_s - \omega_i)$. Carrying out the spatial integration including

the loss terms, imposes the phase-matching condition associated to momentum conservation, which gives the triplet state

$$|\Psi_3\rangle = \left(\frac{2\pi\lambda L}{(\delta k)^3}\right) e^{-(\alpha_p+3\alpha_s)L/4} \sum_{k_r} \sum_{k_s} \sum_{k_i} \Phi(\omega_r, \omega_s, \omega_i) \hat{a}^\dagger(\omega_r) \hat{a}^\dagger(\omega_s) \hat{a}^\dagger(\omega_i) |0\rangle, \quad (26)$$

where the condition $\omega_p = \omega_r + \omega_s + \omega_i$ holds. We have defined the spectral amplitude function

$$\Phi(\omega_r, \omega_s, \omega_i) = \beta(\omega_p) \ell(\omega_r) \ell(\omega_s) \ell(\omega_i) \text{sinc}[\{\Delta k + i\Delta\alpha\}L/4], \quad (27)$$

where the function $\text{sinc}(x) = \sin(x)/x$ is highly peaked at $x = 0$. We have defined the loss mismatch $\Delta\alpha = (\alpha_p - 3\alpha_s)$.

The signal intensity outside the waveguide is proportional to the expectation value $\langle \Psi_3 | \hat{E}^{(-)}(t) \hat{E}^{(+)}(t) | \Psi_3 \rangle$, with electric field operator $\hat{E}^{(+)}(t) \propto i\sqrt{\delta k} \sum_k \ell(\omega) \exp[i\omega t] \hat{a}(k)$, that includes all possible wavevectors k . The detected intensity must be averaged over a specific time interval. The Fourier components of the intensity sum up separately. Since the signal intensity is proportional to the number of photons, we have $N_3 \propto \langle \Psi_3 | \sum_k \hat{a}^\dagger(k) \hat{a}(k) | \Psi_3 \rangle$. Accordingly, the number of triplets per second (generalizing Eq. (19) in Ref. [24]) can be written as

$$\begin{aligned} R_3 &= R \langle \Psi_3 | \sum_k \hat{a}^\dagger(k) \hat{a}(k) | \Psi_3 \rangle \\ &= R \frac{(2\pi\lambda L)^2 (3^2)}{\delta k^3} e^{-(\alpha_p+3\alpha_s)L/2} \iiint_{-\infty}^{\infty} d\omega_r d\omega_s d\omega_i g(\omega_r) g(\omega_s) g(\omega_i) |\Phi(\omega_r, \omega_s, \omega_i)|^2 \end{aligned} \quad (28)$$

where $g(\omega_i) = [\partial k / \partial \omega]_{\omega=\omega_i}$ is a factor resulting from the change of variable from k to ω and R is the repetition rate of the pump. To further simplify the expression for R_3 , we expand the phase mismatch Δk to second order in the signal detuning v_m from the point of PPM $\omega_m^0 = \omega_p/3$, assuming that the pump frequency is fixed at the PPM point. The zeroth and first order terms in the expansion vanish, giving

$$\Delta k = k(\omega_s) + k(\omega_r) + k(\omega_i) - k(\omega_p) = \frac{D_s}{2} [v_r^2 + v_s^2 + (v_s + v_r)^2], \quad (29)$$

where we have eliminated one of the signal detunings (v_i) from the integration using the energy conservation rule. $D_s \equiv \partial^2 k / \partial \omega^2$ is the group velocity dispersion (GVD) of the signal mode, which is the same for the all frequencies in mode-degenerate TOSPDC.

We note that for a Gaussian pump, the peak pump power P_0 is related to the average pump power P and to the repetition rate R by $P_0 = P\sigma/\sqrt{2\pi}R$ and that $|\int d\omega_p \beta(\omega_p)|^2 = \sqrt{2\pi}\sigma$. The dependence on the pump bandwidth σ disappears from the factor outside the integrals characterizing the rate R_3 in Eq. (28), so we can easily take the limit $\sigma \rightarrow 0$ corresponding to continuous wave (cw) pumping to obtain

$$R_3 = \frac{2^2 3^2 \hbar c^3 n_p^3}{\pi^2 (\omega_p^0)^2} \gamma^2 L^2 P \left(\frac{\omega_0}{n_0^2(\omega)} g(\omega_0) \right)^3 \times e^{-(\alpha_p+3\alpha_s)L/2} \iint_{-\infty}^{\infty} dv_r dv_s |\Phi(v_r, v_s)|^2. \quad (30)$$

In the integration we used the approximation $\ell(\omega_0 + v_r) = \ell(\omega_0 + v_s) = \ell(\omega_0 - v_r - v_s) = \ell(\omega_0)$, with $\omega_0 = \omega_p/3$. For notational convenience, we made the replacement

$$\frac{(2\pi\lambda L)^2 3^2}{\delta k^3} = \frac{3^2 (2\pi)^2 \epsilon_0^3 c^3 n_p^3}{\hbar^2 (\omega_p^0)^2} \frac{2\gamma^2 L^2 P}{|\int d\omega_p \beta(\omega_p)|^2}, \quad (31)$$

where γ is the effective nonlinearity from Eq. (15).

In the main text, we also introduced Eq. (7) for estimating the triplet generation rate with losses, not taking into account mode dispersion. The expression can be derived as follows. The number of complete triplets that reach the end of the waveguide after being generated in the segment of the waveguide from z to $z + \Delta z$ can be estimated as

$$\begin{aligned} dN_3(z) &= \tilde{\zeta} N_p(z) e^{-3\alpha_s(L-z)} \Delta z \\ &= \tilde{\zeta} N_{p0} e^{-\alpha_p z} e^{-3\alpha_s(L-z)} dz, \end{aligned} \quad (32)$$

where N_{p0} is the number of pump photons at the input facet of the waveguide. $\tilde{\zeta}$ quantifies the conversion efficiency. Integrating the expression above from $z = 0$ to $z = L$ gives the total number of generated triplets

$$N_3 \equiv \int_0^L dz N_3(z) = \frac{\tilde{\zeta} N_{p0}}{\alpha_p - 3\alpha_s} (e^{-3\alpha_s L} - e^{-\alpha_p L}). \quad (33)$$

Maximizing this expression with respect to L gives the optimal length L_{opt} .

Due to strong light confinement within integrated waveguides and the potential to use high pump powers with materials that have a high damage threshold, two-photon absorption must be considered even for continuous wave pump sources. Multi-photon absorption is described by the relationship

$$\frac{dI(z)}{dz} = -\alpha^{(1)} I(z) - \alpha^{(2)} [I(z)]^2 \quad (34)$$

Where $\alpha^{(1)}$ is single photon loss, $\alpha^{(2)}$ is the two-photon absorption coefficient, and $I(z)$ is the light intensity in the waveguide as a function of position. We can solve Eq. (34) to calculate light intensity as a function of z

$$I(z) = \frac{\alpha I_0 / (\alpha^{(1)} + \alpha^{(2)} I_0)}{e^{\alpha^{(1)} z} - \alpha^{(2)} I_0 / (\alpha^{(1)} + \alpha^{(2)} I_0)} \quad (35)$$

Where I_0 is the initial light intensity inside the waveguide. Intensity relates to the number of photons in a waveguide propagating mode by $N_0 = I_0 A_{\text{mode}} / \hbar \omega_p$ where A_{mode} is the cross-sectional area of the mode. We can rewrite Eq. (32) to include the effect of two-photon absorption

$$dN_3(z) = \frac{\tilde{\zeta} A_{\text{mode}} I_{p0}}{\hbar \omega_p} \frac{\alpha_p^{(1)} / (\alpha_p^{(1)} + \alpha_p^{(2)} I_{p0})}{e^{\alpha_p^{(1)} z} - \alpha_p^{(2)} I_{p0} / (\alpha_p^{(1)} + \alpha_p^{(2)} I_{p0})} e^{-3\alpha_s^{(1)}(L-z)} dz. \quad (36)$$

We can use the ratio of Eq. (36) and (32) to gain insight under which conditions two-photon absorption has a significant impact on device performance. We define an arbitrary threshold

$$\frac{\alpha_p^{(2)} I_{p0}}{\alpha_p^{(1)}} (1 - e^{-\alpha_p^{(1)} L_{\text{opt}}}) < 0.2 \quad (37)$$

below which the impact of two-photon absorption decreases the photon triplet generation rate by less than 10%. For our proposed TiO₂ devices, this corresponds to $\alpha_p^{(1)} > 10$ dB/cm, a maximum pump power of approximately 1 W, and $\alpha_p^{(2)} = 3$ cm/GW (determined by band-gap scaling [30] of two-photon absorption measured in the wavelength range 780 – 1560 nm [19]).

D. Coincidence detection signals

The temporal coherence of a triplet source is characterized by the third-order intensity correlation function

$$G^{(3)}(x_1, x_2, x_3) = \langle \Psi_3 | E^{(-)}(x_1) E^{(-)}(x_2) E^{(-)}(x_3) E^{(+)}(x_3) E^{(+)}(x_2) E^{(+)}(x_1) | \Psi_3 \rangle. \quad (38)$$

where $|\Psi_3\rangle$ is the triplet state defined in Eq. (26). For waveguides much longer than a typical signal wavelength, we can replace the wave vector summations by frequency integrals. Energy conservation allows us to eliminate one of the signal variables from the integration. We can also absorb physical parameters like the cw pump amplitude, the effective waveguide area and the material nonlinear susceptibility into a normalization factor that depends on the waveguide length L . We assume a narrow cw pump at fixed frequency ω_p . The triplet state is completely characterized by the spectral amplitude $\Phi(\omega_r, \omega_s)$ in Eq. (27). The loss mismatch parameter $\Delta\alpha \equiv (\alpha_p - 3\alpha_s)$ introduces a frequency-dependent imaginary part to the spectral amplitude, which broadens the triplet state in the frequency domain. The $G^{(3)}$ function in Eq. (38) can be written in simplified form as

$$G^{(3)}(x_1, x_2, x_3) = |\psi(x_1, x_2, x_3)|^2, \quad (39)$$

where $\psi(x_1, x_2, x_3) = \langle 0 | E^{(+)}(x_3) E^{(+)}(x_2) E^{(+)}(x_1) | \Psi_3 \rangle$ is the so-called triphoton state [16], which can be written as

$$\begin{aligned} \psi(x_1, x_2, x_3) = & \int d\omega_1 d\omega_2 d\omega_3 \int d\omega_r d\omega_s f_1(\omega_1) f_2(\omega_2) f_3(\omega_3) e^{-i\omega_1 x_1 - i\omega_2 x_2 - i\omega_3 x_3} \\ & \times \Phi(\omega_r, \omega_s) \langle 0 | a(\omega_1) a(\omega_2) a(\omega_3) a^\dagger(\omega_r) a^\dagger(\omega_s) a^\dagger(\omega_p - \omega_r - \omega_s) | 0 \rangle. \end{aligned} \quad (40)$$

We assume Gaussian detector filters $f_j(\omega) = f_0 \exp[-(\omega - \omega_j)^2 / 2\sigma_j^2]$, where f_0 is a normalization constant and ω_j is the center frequency of the j -th spectral filter. All filters are assumed to have the same bandwidth $\sigma_k = \sigma$. We ignore the frequency-independent normalization factor of the state.

The correlation function $\langle 0 | a(\omega_1) a(\omega_2) a(\omega_3) a^\dagger(\omega_r) a^\dagger(\omega_s) a^\dagger(\omega_p - \omega_r - \omega_s) | 0 \rangle$ in Eq. (40) contains six terms corresponding to permutations of the frequency variables. We can interpret each term by labelling a photon in the triplet source by its frequency. There are thus $3! = 6$ ways for these photons to reach three photodetectors. If the optical paths from the triplet source to each detector are indistinguishable, then all six frequency permutations give the same contribution to the field correlation function. It thus suffices to compute a single permutation to study the triple coincidence signal. We choose $\omega_1 = \omega_r$, $\omega_2 = \omega_s$, and $\omega_3 = \omega_p - \omega_r - \omega_s$ to obtain

$$\psi(x_1, x_2, x_3) = e^{-i\omega_p x_3} \iint d\omega_r d\omega_s f(\omega_r) f(\omega_s) f(\omega_p - \omega_r - \omega_s) \Phi(\omega_r, \omega_s) e^{-i\omega_r(x_1 - x_3) - i\omega_s(x_2 - x_3)}. \quad (41)$$

We expand the frequencies as $\omega_m = \Omega_m + v_m$, with $m = \{r, s, i\}$, around central signal frequencies Ω_m that satisfy the energy conservation rule $\omega_p = \omega_r + \omega_s + \omega_i$ at the PPM point. In what follows we consider that the spectral filter $f(\omega_m)$ is centered at the frequency Ω_m . Expanding the wavenumbers to second order in the frequency detunings v_m around the PPM point gives a phase mismatch Δk as in Eq. (29). For mode-degenerate down-conversion the group velocities are equal for the three photons, making the linear term vanish by energy conservation for a cw pump. We can rewrite the integrals in terms of frequency detunings to obtain

$$G^{(3)}(x_1, x_2, x_3) = \left| \int dv_r dv_s f_r(v_r) f_s(v_s) f_i(v_r + v_s) \Phi(v_r, v_s) e^{-iv_r(x_1 - x_3) - iv_s(x_2 - x_3)} \right|^2. \quad (42)$$

The numerical evaluation of the integral is simplified by rescaling the detunings and delay times as v_n/v_0 and x_n/τ_0 , where $\tau_0 = \sqrt{D_s L}/2$ and $v_0 = 1/\tau_0$ are the characteristic frequency and timescale associated with a waveguide of length L and group velocity dispersion D_s of the signal guiding mode.

The two-photon coincidence detection signal is proportional to the second-order correlation function

$$G^{(2)}(x_1, x_2) = \langle \hat{E}^{(-)}(x_1) \hat{E}^{(-)}(x_2) \hat{E}^{(+)}(x_2) \hat{E}^{(+)}(x_1) \rangle, \quad (43)$$

which can be written by inserting the resolution of the identity in the Fock basis as

$$G^{(2)}(x_1, x_2) = \int d\omega_3 |\langle 0 | a(\omega_3) E^{(+)}(x_2) E^{(+)}(x_1) | \Psi_3 \rangle|^2, \quad (44)$$

with a wavepacket amplitude given by

$$\begin{aligned} \langle 0 | a(\omega_3) E^{(+)}(x_2) E^{(+)}(x_1) | \Psi_3 \rangle &= \int d\omega_1 d\omega_2 \int d\omega_r d\omega_s \Phi(\omega_r, \omega_s) f(\omega_1) f(\omega_2) e^{-i\omega_1 x_1 - i\omega_2 x_2} \\ &\quad \times \langle 0 | a(\omega_3) a(\omega_1) a(\omega_2) a^\dagger(\omega_r) a^\dagger(\omega_s) a^\dagger(\omega_p - \omega_r - \omega_s) | 0 \rangle. \end{aligned}$$

The evaluation of the vacuum correlation function gives $2! = 4$ non-zero terms associated with the commutation of the operators $a(\omega_1)$ and $a(\omega_2)$ with $a(\omega_r)$ and $a(\omega_s)$. These four terms can be made equal to each other by exchanging integration variables appropriately when the optical paths to the detectors are equal. We thus evaluate a single representative term, corresponding to $\omega_1 = \omega_r$ and $\omega_2 = \omega_s$ to obtain

$$G^{(2)}(x_1, x_2) = \int dv_3 \left| \int dv_r G(v_r, v_r + v_3) f_1(v_r) f_2(v_r + v_3) e^{-iv_r(x_1 - x_2)} \right|^2. \quad (45)$$

Acknowledgments

MGM and FH are co-first authors of the manuscript. CCE proposed to use TiO₂ for TOSPD. MGM, CCE, FH and OR developed the description of phase matching in integrated devices. MGM, SG-N and OR developed the mode overlap calculations and device design methods. OR fabricated waveguides and MGM, SG-N, and OR completed measurements of THG. FH and GGG developed the quantum theory of lossy TOSPD. FH performed stochastic wavefunction simulations and derived the entanglement witness for non-degenerate TOSPD. EM and AA-G supervised the research and manuscript preparation. All authors approved the final copy of the manuscript. Benjamin Franta and Philip Muñoz provided feedback on the manuscript throughout its development. We acknowledge support from the NSF Division of Physics under contract PHY-1415236, the Harvard Quantum Optics Center, the Natural Sciences and Engineering Research Council of Canada, the NSF Graduate Research Fellowship Program (DGE1144152), and Harvard CNS. FH thanks support from DTRA HDTRA 1-100109946 and the CONICYT programs PAI 79140030 and Iniciación 11140158. CCE acknowledges support from the Kavli Institute at Cornell for Nanoscale Science.